

# Metal-alcohol coordination promoted reduction of bismuth (III) in bismuth-based semiconductors for enhanced photocatalytic activity

Haiping Li<sup>a</sup>, Guoan Wang<sup>a</sup>, Quanhua Deng<sup>a,b</sup>, Wenxuan Hu<sup>a</sup>, Wanguo Hou<sup>a,\*</sup>

<sup>a</sup> National Engineering Research Center for Colloidal Materials, School of Chemistry and Chemical Engineering, Shandong University, Jinan, Shandong 250100, China

<sup>b</sup> Stanley fertilizer (plain) Co., Ltd, Dezhou, Shandong 253000, China



## ARTICLE INFO

### Keywords:

Photocatalysis

Bismuth

Oxygen vacancy

Metal-alcohol coordination

Nitrogen fixation

## ABSTRACT

Metal ion doping is an extensively researched method to enhance photocatalytic activity of bismuth-based semiconductors, but function of the metal ions need be further clarified. Herein, metal-alcohol coordination was evidenced to promote reduction of Bi<sup>III</sup> in Bi-based semiconductors (e.g., Bi<sub>2</sub>MoO<sub>6</sub> hierarchical micro-spheres) to generated oxygen vacancies (Ovs) and Bi metal (Bi<sup>0</sup>). Ovs and Bi<sup>0</sup>, rather than widely recognized doping metal ions, play a key role for remarkable enhancement of photocatalytic activity of Bi<sub>2</sub>MoO<sub>6</sub>, for example of ~16-fold higher photocatalytic nitrogen reduction activity, which arises from that the Ovs and Bi<sup>0</sup> can enhance photoexcited charge separation and work as surface active sites. The Ovs possess much greater efficacy than the Bi<sup>0</sup>. Formation of Bi<sup>0</sup> also induces prominent morphological variation of the microspheres. This work discloses an interesting but neglected phenomenon in alcohoothermal synthesis of “metal-doped” Bi-based semiconductors and aims at drawing high attention of relevant researchers.

## 1. Introduction

Photocatalytic solar conversion to decrease fossil energy consumption and environmental contamination requests efficient photocatalysts. Bi-based semiconductors (e.g., Bi<sub>2</sub>MoO<sub>6</sub>, Bi<sub>x</sub>O<sub>y</sub>N (N = Cl, Br, or I), and Bi<sub>2</sub>WO<sub>6</sub>) are a kind of widely researched photocatalysts, with advantages of low cost, ease in synthesis, wide availability of feedstocks, and visible-light response (except BiOCl), and have been used in various photocatalytic reactions, such as nitrogen fixation, contaminant degradation, water splitting, and CO<sub>2</sub> reduction [1–5], but their photocatalytic activity need be considerably enhanced for practical application.

Surface area enlargement and elemental doping were commonly used strategies to enhance photoactivity of Bi-based semiconductors [1, 3], and morphological regulation, i.e., building hierarchical structures (e.g., microspheres and microflowers [6,7]) by solvothermal synthesis is the most used and simplest way to increase the surface areas. In the solvothermal synthesis, used organic solvents are generally alcohols (e.g., ethylene glycol (EG), methoxyethanol, and glycerol) [8–10], in view of strong coordination between Bi<sup>III</sup> and hydroxyls in alcohol molecules to increase solubility of Bi<sup>III</sup> salts [11], but high reducibility of alcohols at high temperature generally results in reduction of Bi<sup>III</sup> and formation

of oxygen vacancies (Ovs, or Bi<sup>3-x</sup>) [12,13] that, however, were overlooked in some photocatalytic research, and thus probable influences of the Ovs on the photocatalytic performance were neglected.

In recent years, simultaneous morphological regulation and metal ion doping in Bi-based semiconductors, realized by alcohoothermal synthesis, drew more interest of scientists owing to their higher efficacy in enhancing photocatalytic performance [14,15], as shown by searchable > 40 papers (Table S1). In some papers, metal ion (e.g., Ni<sup>2+</sup>, Zn<sup>2+</sup>, La<sup>3+</sup>, and Fe<sup>3+</sup>) doping was mentioned to promote Ov generation in the semiconductors (e.g., BiOBr, BiOI, Bi<sub>5</sub>O<sub>7</sub>I, and BiOCl [9,14,16–19]). However, as the metal ion doping was focused on, interactions of metal ions with alcohol molecules and resultant structural variation of products have never been considered, which leads to some false conclusions. Therefore, function of metal ions in alcohoothermal (or even reducing-solvothermal) synthesis of “metal doped” Bi-based semiconductors need be deeply researched, so as to guide synthesis of efficient Bi-based photocatalysts.

In this work, metal ions with exposed d orbitals (e.g., Fe<sup>3+</sup> ions) are evidenced to promote generation of Ovs and even Bi metal (Bi<sup>0</sup>) in Bi-based semiconductors (e.g., Bi<sub>2</sub>MoO<sub>6</sub> (BMO), to form Bi<sup>0</sup>/BMO-Ov core/shell microspheres) in alcohoothermal processes, by coordinating with alcohol hydroxyls to enhance reducibility of the alcohol molecules

\* Corresponding author.

E-mail address: [wghou@sdu.edu.cn](mailto:wghou@sdu.edu.cn) (W. Hou).

(Fig. 1).  $\text{Bi}^0/\text{BMO-Ov}$  exhibits enhanced photogenerated charge separation and thus improved photocatalytic nitrogen reduction reaction (PNRR) activity, benefitting from Ovs and  $\text{Bi}^0$  that can capture photo-excited electrons and work as surface active centers. This work discloses the neglected role of metal ions in alcoothermal synthesis of “metal-doped” Bi-based semiconductors.

## 2. Experimental section

### 2.1. Synthesis of $\text{Bi}^0/\text{BMO-Ov}$ and BMO

A series of  $\text{Bi}^0/\text{BMO-Ov}$  (denoted as  $\text{B}/\text{Fe}\varphi$ , where  $\varphi$  mmol is amount of added  $\text{Fe}^{3+}$  ions) and bulk BMO photocatalysts were synthesized. For synthesis of  $\text{B}/\text{Fe}\varphi$ ,  $\text{FeCl}_3$  ( $\varphi$  mmol ( $\varphi = 0.02, 0.06, 0.1, 0.2, 0.3$  or  $0.4$ ), 99.9%, Aladdin, China) was dissolved in ethylene glycol (EG, 60 mL, 99%, Aladdin), and then  $\text{Bi}(\text{NO}_3)_3 \cdot 5 \text{ H}_2\text{O}$  (2 mmol, 99.99%, Aladdin) and  $\text{Na}_2\text{MoO}_4 \cdot 2 \text{ H}_2\text{O}$  (1 mmol, 99.95%, Aladdin) were successively dissolved in above solution under magnetic stir. The solution was transferred into an 80-mL Teflon-lined autoclave and heated at  $160^\circ\text{C}$  for 12 h in an oven (DHG-9030A, Zhongyigouke, Beijing, China). After cooled naturally to room temperature, the solid product was collected by filtration, washed with water and ethanol three times, and dried at  $60^\circ\text{C}$  for 12 h in the oven. Bulk BMO ( $\varphi = 0$ ) was synthesized similarly as  $\text{B}/\text{Fe}\varphi$ , but without addition of  $\text{FeCl}_3$ .

Synthetic procedures of other samples and details for characterizations and density functional theory (DFT) calculations are shown in the supporting information (S1 – S8).

### 2.2. PNRR tests

The sample (50 mg) was dispersed in ultrapure water (80 mL, obtained from a Merck Milli-Q® IQ 7005 water purification system, Germany) by ultrasonication for 2 min and then transferred into a reactor with temperature controlled at  $20^\circ\text{C}$  by a circulating water-cooling system. The dispersion was purged with  $\text{N}_2$  ( $300 \text{ mL min}^{-1}$ , Jinan Deyang Special Gas Co., Ltd, China) for 30 min to remove oxygen. Then, a 300-W Xe lamp (CEL-HXF300-T3, Ceaulight, China) equipped with a cutoff filter ( $\lambda \geq 420 \text{ nm}$ ) was used as the visible light source to start the reaction. Every 20 min, the dispersion ( $\sim 4.2 \text{ mL}$ ) was taken out and

filtered through a 0.22- $\mu\text{m}$  nylon membrane. The ammonia concentration in the filtrate was measured by the Nessler's reagent spectrophotometry method (S9 and Fig. S1).

In the cyclic experiment of  $\text{B}/\text{Fe}0.2$ , ultrapure water might be replaced with a methanol (99.9%, Aladdin) aqueous solution (10 vol%). After every run, the photocatalyst was collected by filtration, washed with water three times, dried at  $60^\circ\text{C}$  for 12 h in the oven, and used in the next run.

To determine the external quantum yield (EQY) of  $\text{B}/\text{Fe}0.2$  at 420 nm, a 420-nm band-pass filter (Thorlabs, USA) was substituted for above cutoff filter and the EQY was calculated by the equation,  $\text{AQY} = 3R_N/(E_i A/E_p) \times 100\%$ , where  $R_N$  is the  $\text{NH}_3$  generation rate ( $\text{mol s}^{-1}$ ),  $A$  is the illumination area ( $\text{cm}^2$ ),  $E_i$  is the incident light intensity minus the transmission light intensity ( $\text{W cm}^{-2}$ ), and  $E_p$  is the photon energy ( $\text{J mol}^{-1}$ ). Values of  $A$  and  $E_i$  were measured to be  $3.46 \text{ cm}^{-2}$  and  $0.0171 \text{ W cm}^{-2}$ , respectively.

### 2.3. Photocatalytic pollutant degradation tests

Photocatalytic degradation toward a model pollutant, Rhodamine B (RhB) was carried out on an XPA-7 photocatalytic reaction equipment (Xujiang Electromechanical Factory, China) [20]. The visible light source is a 400-W metal halide lamp equipped with an ultraviolet cut-off filter ( $\lambda \geq 420 \text{ nm}$ ). Infrared light is absorbed by a water filter around the lamp, and the distance between the lamp and the reaction tube is  $\sim 10 \text{ cm}$ . The reaction tube is immersed in a water bath of which the temperature was maintained at  $< 20^\circ\text{C}$ . For each tube, the sample (50 mg) was dispersed in a RhB (95%, Aladdin) aqueous solution ( $10 \text{ mg L}^{-1}$ , 50 mL) and magnetically stirred in the dark for 1 h to reach the sorption equilibrium. During irradiation, the suspension (4 mL) was taken out every one hour, rested for 24 h, and filtered through a 0.45- $\mu\text{m}$  poly(ether sulfone) syringe filter, with the filtrate analyzed on an UV-1800 spectrophotometer (Shimadzu, Japan) at the wavelength of 554 nm.

In the cyclic experiment, the photocatalyst was collected by filtration, washed with water three times, dried at  $60^\circ\text{C}$  for 12 h, and used in the next run.

In the quenching experiments of active species, p-benzoquinone (99%, Aladdin), sodium oxalate (99.99%, Aladdin), and t-butanol

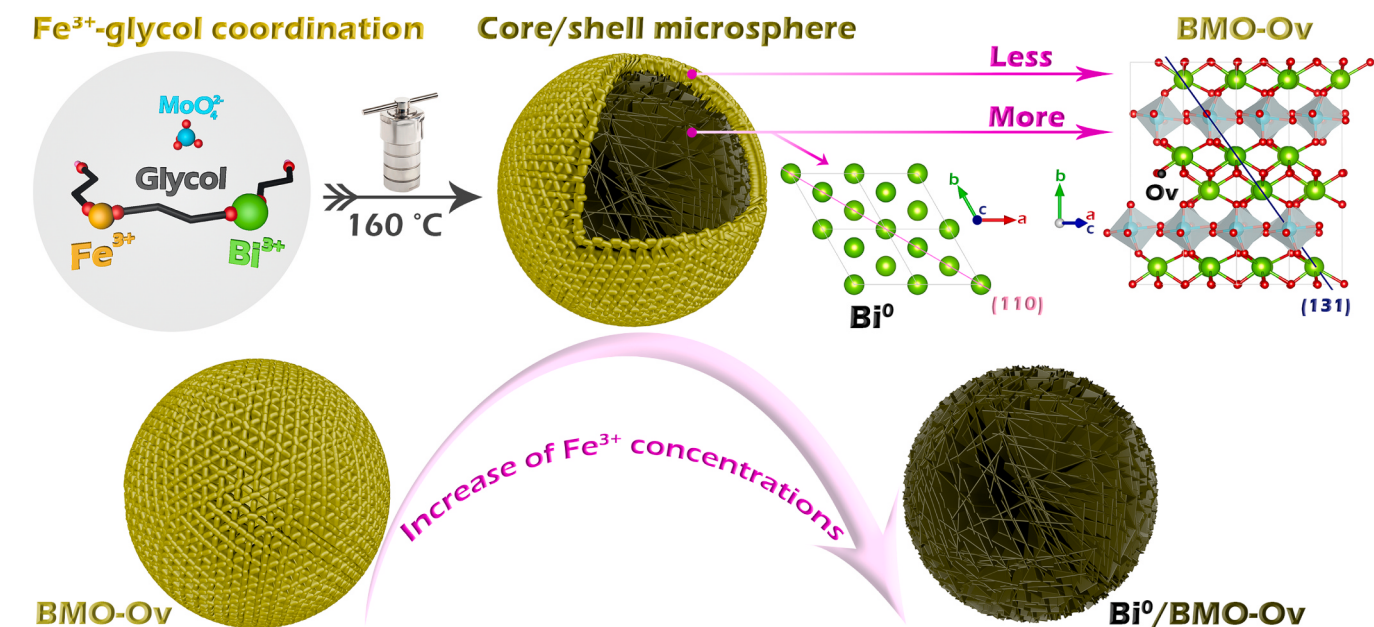


**Fig. 1.** (a) Schematic illustration for synthesis of  $\text{Bi}^0/\text{BMO-Ov}$  core/shell hierarchical microspheres, structures of precursors and products, and structural evolution from  $\text{BMO-Ov}$  to  $\text{Bi}^0/\text{BMO-Ov}$  microspheres with the increase of added  $\text{Fe}^{3+}$  concentrations.

(99.5%, Aladdin) were used as scavengers and added to suspensions in reaction tubes (0.2, 0.4, and 40 mmol L<sup>-1</sup>) to quench superoxide radicals (-O<sub>2</sub><sup>-</sup>), holes, and hydroxyl radicals (-OH), respectively.

### 3. Result and discussion

#### 3.1. Compositions, morphologies, and structures of Bi<sup>0</sup>/BMO-Ov

BMO comprises hierarchical microspheres composed of small irregular nanoplates, and interestingly, with the increase of  $\varphi$  from 0.06 to 0.4, B/Fe $\varphi$  exhibits morphological transformation from nanoplate-composed to nanosheet-composed hierarchical microspheres (Fig. 2a–c, S2 and S3), with nanosheet/nanoplate core/shell hierarchical microspheres distinctly observed in B/Fe0.2 (Fig. 2b and S4), which suggests a significant effect of added FeCl<sub>3</sub>. The high-resolution transmission electron microscopy (HRTEM) image of B/Fe0.2 shows distinct lattice fringes with spacing of 3.14 Å, corresponding to (131) facets of orthorhombic Bi<sub>2</sub>MoO<sub>6</sub> (JCPDS No. 21-0102), and that with spacing of 2.26 Å, corresponding to the (110) facet of hexagonal Bi<sup>0</sup> (JCPDS No. 85-1329) [21,22] (Fig. 2d), suggesting formation of the nanosheet-composed microspheres likely results from generation of Bi<sup>0</sup> that originates from the FeCl<sub>3</sub> effect. Energy dispersive X-ray spectroscopy (EDS) spectra of the core/shell microspheres in B/Fe0.2 (Fig. 2e) clearly show existence of Bi, Mo, O, and Fe elements in both the core and the shell, suggesting Fe residual in the product. Gained Bi/Mo and Fe/Mo ratios in the core (3.27 and 0.37) are remarkably greater than those in the shell (2.38 and 0.28) and the Bi/Mo ratios are greater than that of BMO (2.09, Fig. S5), suggesting Bi<sup>0</sup> was generated from the core and this process was promoted by FeCl<sub>3</sub>.

EDS line-scanning on the core/shell microsphere was performed to further determine their elemental compositions. As shown in Fig. 2f, from the shell to the core, content of Bi and Mo elements increases and that of the O element slightly decreases, which indicates generation of more Ovs in the core than in the shell (see analysis in S10). Overall, Bi<sup>0</sup> and Ovs were concomitantly generated in the core/shell microsphere and it is the gradually increased Bi<sup>0</sup> content in the core that results in the morphological transformation from BMO to B/Fe0.4 (with the increase of added Fe<sup>3+</sup> amount) (Figs. 1 and 2a–c).

X-ray diffraction (XRD) patterns of BMO and B/Fe $\varphi$  were measured to determine their crystallinity. As shown in Fig. 3a, diffraction peaks BMO are well indexed to orthorhombic Bi<sub>2</sub>MoO<sub>6</sub> (JCPDS No. 21-0102), but those of B/Fe $\varphi$  are also indexed to hexagonal Bi<sup>0</sup> (JCPDS No. 85-1329) [21,22], beside the orthorhombic Bi<sub>2</sub>MoO<sub>6</sub>. The peaks of Bi<sup>0</sup> in B/Fe $\varphi$  gradually strengthen with the increase of  $\varphi$ , potently indicating FeCl<sub>3</sub>-promoted generation of Bi<sup>0</sup>. When FeCl<sub>3</sub> was replaced with Fe (NO<sub>3</sub>)<sub>3</sub> in synthesis of B/Fe0.2, Bi<sup>0</sup> was still generated (Fig. S6), but when NaCl or NaNO<sub>3</sub> was substituted for FeCl<sub>3</sub>, Bi<sup>0</sup> was not formed (Fig. S7), manifesting generation of Bi<sup>0</sup> originates from Fe<sup>3+</sup> ions, rather than their counterions. When FeCl<sub>3</sub> was replaced with Bi(NO<sub>3</sub>)<sub>3</sub>, no Bi<sup>0</sup> was generated; when Na<sub>2</sub>MoO<sub>4</sub> was not added, Bi<sup>0</sup> was still generated, and when Na<sub>2</sub>MoO<sub>4</sub> and FeCl<sub>3</sub> were not added, XRD peaks of generated Bi<sup>0</sup> turn weak; even though Fe<sup>3+</sup> ions were substituted for Bi<sup>III</sup> ions, Bi<sup>0</sup> was still generated (Fig. S8). These further demonstrate generation of Bi<sup>0</sup> results from Fe<sup>3+</sup> ions, rather than Bi<sup>III</sup> and MoO<sub>4</sub><sup>2-</sup> ions. The solvent effect was further investigated (Fig. S9) and in the order, ethanol → EG → glycerol, XRD peaks of Bi<sup>0</sup> gradually strengthen, while Bi<sup>0</sup> was not generated in water, which indicates Bi<sup>0</sup> was generated via alcohol reduction of Bi<sup>III</sup> and high hydroxyl density can expedite Bi<sup>0</sup> generation.

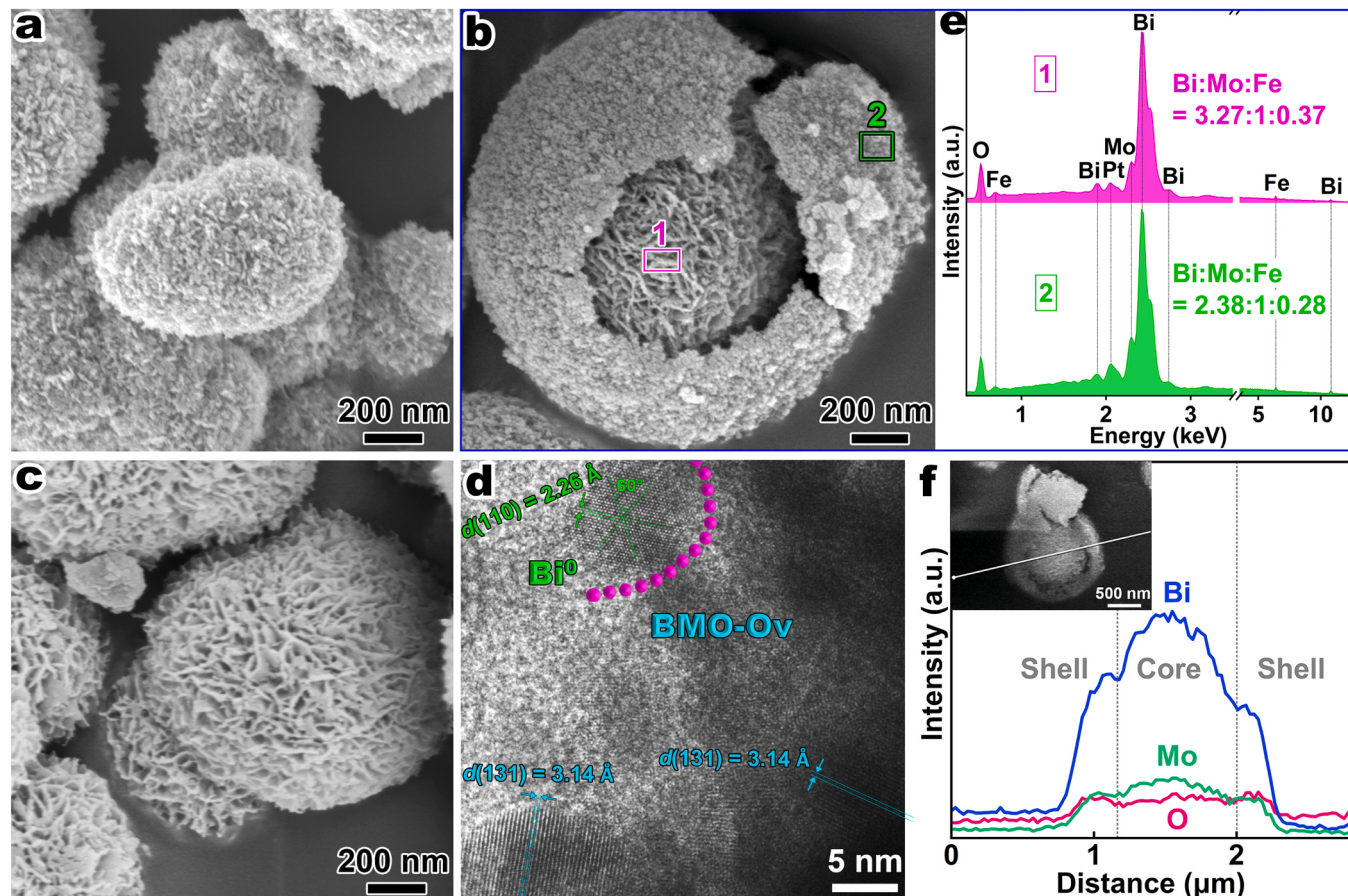
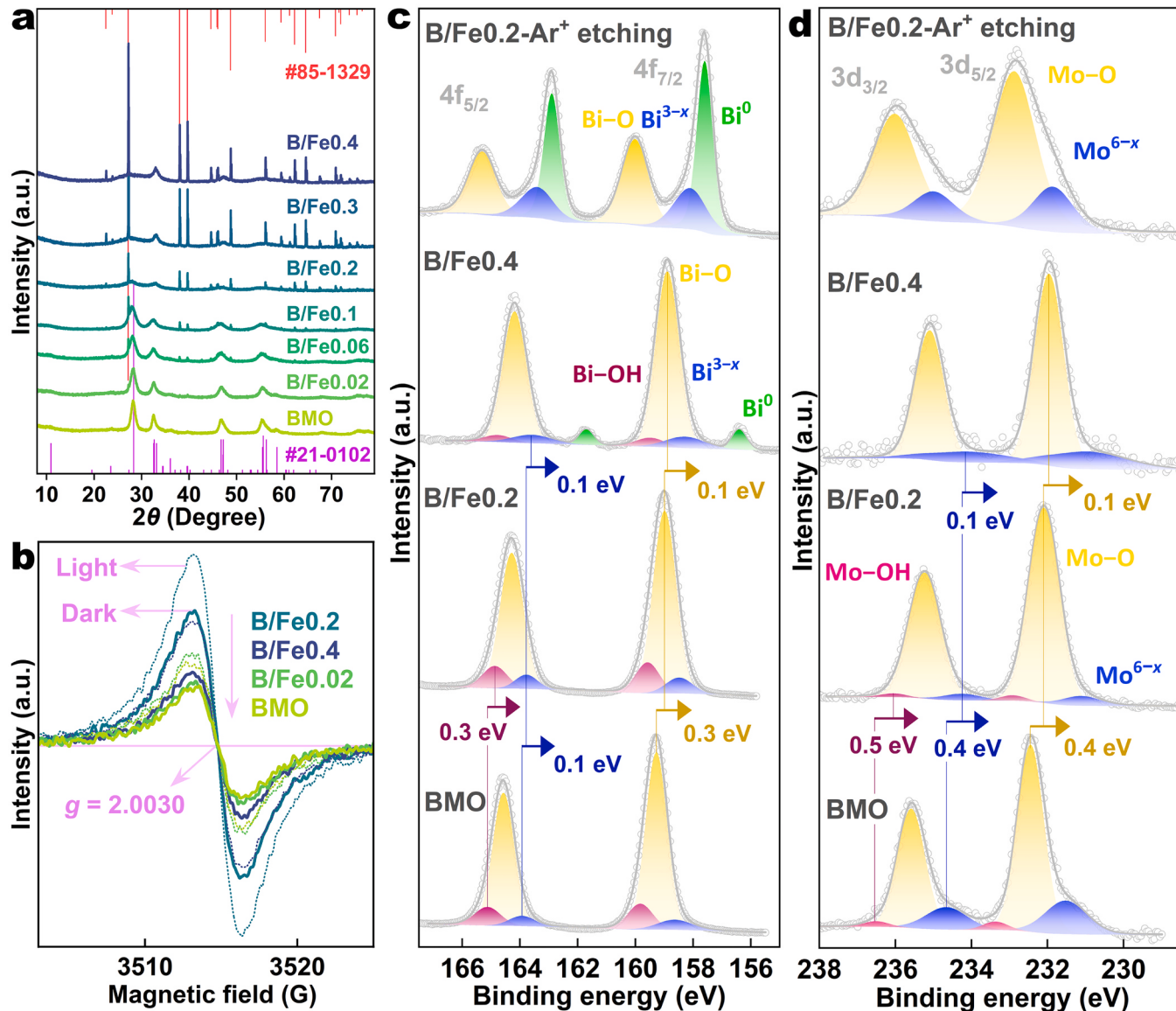


Fig. 2. SEM images of (a) BMO, (b) B/Fe0.2, and (c) B/Fe0.4; (d) the HRTEM image of B/Fe0.2; (e) the EDS spectra of B/Fe0.2 in marked areas in (b) with elemental molar ratios provided; and (f) EDS line-scanning on a (inset) core-shell microsphere in B/Fe0.2.



**Fig. 3.** (a) XRD patterns of BMO and B/Fe $\varphi$ ; (b) EPR spectra of samples in dark and under light irradiation; and (c) Bi 4 f and (d) Mo 3d core-level XPS spectra of samples.

Overall, generation of Bi<sup>0</sup> originates from Fe<sup>3+</sup> ions that, functioning as catalysts, enhance reducibility of alcohol molecules.

Electron paramagnetic resonance (EPR) spectroscopy was performed to detect Ovs in BMO and B/Fe $\varphi$  (Bi<sup>0</sup> is EPR silent [23,24]). As shown in Fig. 3b, all the spectra show one single Lorentzian lines centering at  $g$  of 2.0030, corresponding to Ovs [25], and the signals strengthen then weaken with the increase of  $\varphi$  both in dark and under light irradiation, indicating an increase then decrease of Ovs in the samples, with B/Fe0.2 containing the most Ovs, which means Fe<sup>3+</sup> ions promoted generation of Ovs and Bi<sup>0</sup> was further generated from the Ovs, considering B/Fe0.4 possesses the most Bi<sup>0</sup>. In addition, B/Fe0.2 exhibits the weakest XRD peaks of Bi<sub>2</sub>MoO<sub>6</sub> phase among B/Fe $\varphi$  (Fig. 3a), indicative of the lowest crystallinity induced by its most Ovs, which can also be proved by gradual increase of the crystal facet distance [12] from BMO to B/Fe0.2 (Fig. S10).

X-ray photoelectron spectroscopy (XPS) was further carried out to determine structures of the samples. The Bi 4 f core-level XPS spectrum of BMO shows three couples of peaks at binding energy of 165.1 and 159.8 eV, 164.6 and 159.3 eV, and 163.9 and 158.6 eV (Fig. 3c), assigned to surface Bi-OH, Bi-O, and Ovs (Bi<sup>3-x</sup>), respectively [12,26],

and its Mo 3d XPS spectrum also shows three couples of peaks at 236.5 and 233.4 eV, 235.6 and 232.5 eV, and 234.6 and 231.5 eV (Fig. 3d), assigned to surface Mo-OH, Mo-O, and Ovs (Mo<sup>6-x</sup>), respectively [12,26]. Ovs in BMO were formed by EG reduction of Bi<sup>III</sup>. Similarly, the Bi 4 f XPS spectrum of B/Fe0.2 shows the three couples of peaks corresponding to Bi-OH, Bi-O, and Bi<sup>3-x</sup>, but the peaks relatively shift to low binding energy by 0.3, 0.1, and 0.3 eV, respectively (Fig. 3c), and its Mo 3d XPS spectrum shows the three couples of peaks, corresponding to Mo-OH, Mo-O, and Mo<sup>6-x</sup>, which relatively shift to low binding energy by 0.5, 0.4, and 0.4 eV, respectively (Fig. 3d). The Bi 4 f spectrum of B/Fe0.4 also shows the three couples of peaks, but with ~0.1-eV shift to low binding energy, relative to the peaks of B/Fe0.2, and quite differently, the Bi 4 f spectrum shows another couple of peaks at binding energy of 161.7 and 156.4 eV (Fig. 3c), assigned to Bi metal [27], effectively indicating generation of Bi<sup>0</sup>. The Mo 3d spectrum of B/Fe0.4 only shows two couples of peaks (Fig. 3d), corresponding to Mo-O and Mo<sup>6-x</sup>, which shift ~0.1 eV to low binding energy, relative to those of Bi/Fe0.2. There was not Mo<sup>0</sup> generated in the sample. Remarkable shift of peaks in Bi 4 f and Mo 3d spectra of B/Fe0.2 and B/Fe0.4 suggest influences of generated Ovs and Bi<sup>0</sup> that are relatively rich in electrons.

Interestingly,  $\text{Bi}^0$  peaks were not gained for B/Fe0.2 by deconvolution, with B/Fe0.2 and BMO exhibiting similar Bi/Mo molar ratios (XPS detection depth is  $<10$  nm), while B/Fe0.4 exhibits prominent  $\text{Bi}^0$  peaks and a higher Bi/Mo molar ratio (Table S2), suggesting  $\text{Bi}^0$  distributes mainly in the core of B/Fe0.2 core/shell microspheres, consistent with the SEM and EDS results.

After  $\text{Ar}^+$  etching, the Bi 4 f spectrum of B/Fe0.2 shows three couples of peaks at 165.3 and 160.0 eV, 163.4 and 158.1 eV, and 162.9 and 157.6 eV (Fig. 3c), that should be assigned to  $\text{Bi}-\text{O}$ ,  $\text{Bi}^{3-x}$ , and  $\text{Bi}^0$ , respectively, while its Mo 3d spectrum shows only two couples of peaks at 236.0 and 232.9 eV, and 235.0 and 231.9 eV (Fig. 3d), assigned to  $\text{Mo}-\text{O}$  and  $\text{Mo}^{6-x}$ , without  $\text{Mo}^0$  generated in the sample.  $\text{Ar}^+$ -etched B/Fe0.2 exhibits much stronger  $\text{Bi}^0$  peaks than B/Fe0.4, suggesting  $\text{Bi}^0$

distributes mainly in the inside of the cores.  $\text{Ar}^+$ -etched B/Fe0.2 and B/Fe0.4 exhibit higher  $\text{Bi}^{3-x}$  content (21 and 9 at%) than BMO (7 at%), while similar  $\text{Mo}^{6-x}$  content ( $20 \pm 1$  at%) as BMO (Table S2), consistent with the EPR results, indicating  $\text{Fe}^{3+}$ -induction formed Ovs lie mainly at Bi atoms. The disappearance of Mo-OH peaks of B/Fe0.4 and  $\text{Ar}^+$ -etched B/Fe0.2 suggest dominant distribution of Bi element in surface layers, owing to formation of  $\text{Bi}^0$  and  $\text{Bi}^{3-x}$ . O 1 s core-level XPS spectra also indicate Ov and  $\text{Bi}^0$  induced relative peak shift (Fig. S11). Fe 2p and Cl 2p core-level spectra of B/Fe0.2 and B/Fe0.4 indicate residual of Fe and Cl ions in the samples (Fig. S12). Overall,  $\text{Fe}^{3+}$ -enhanced reducibility of alcohol molecules leads to generation of Ovs at Bi atoms and  $\text{Bi}^0$ .

The synergism of  $\text{Fe}^{3+}$  ions and EG can also promote generation of

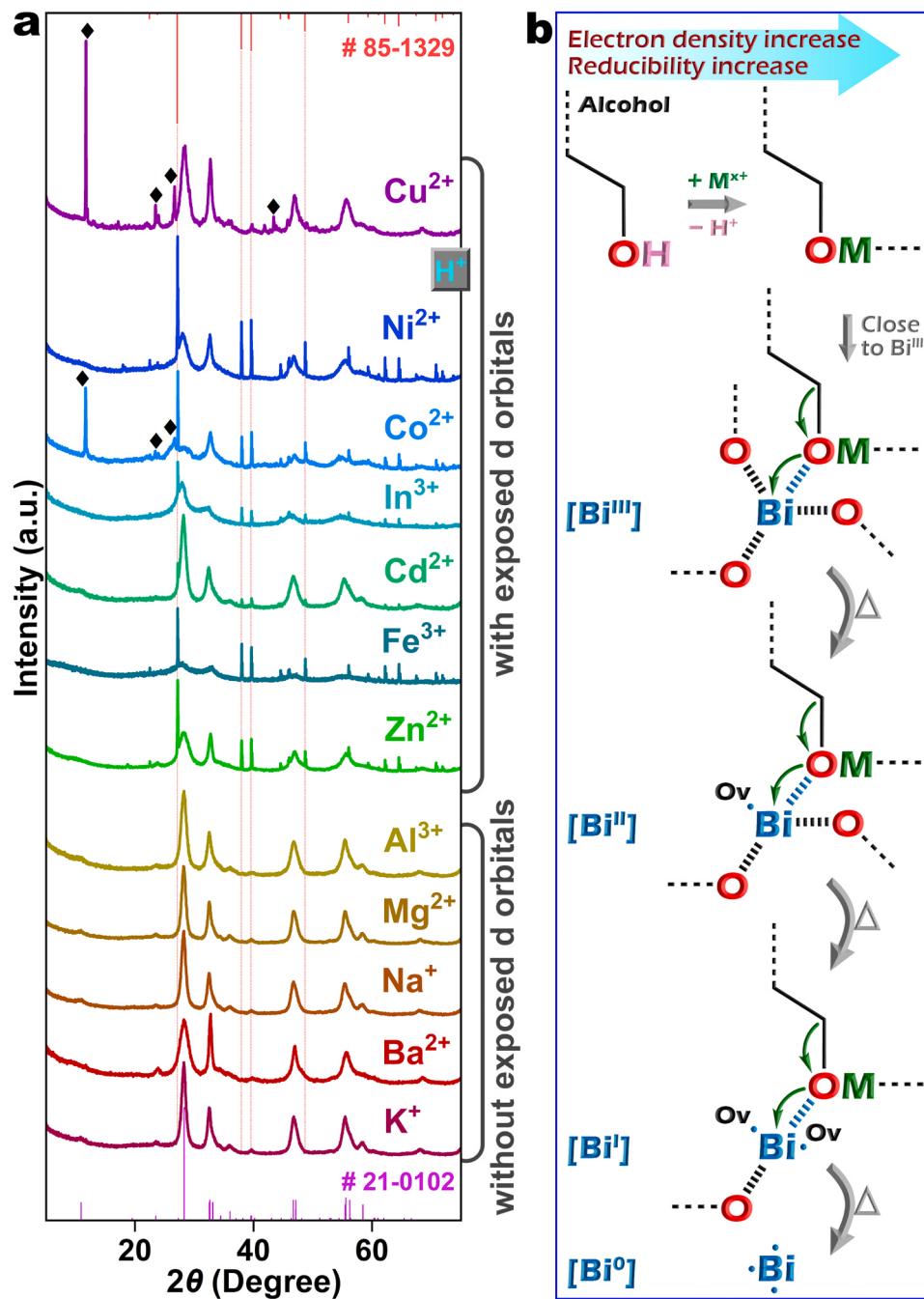


**Fig. 4.** (a) XRD patterns of B/Fe0.2 and samples synthesized similarly as B/Fe0.2, but with  $\text{Fe}^{3+}$  ions replaced by various metal ions; and (b) schematic illustration for metal-alcohol coordination and progressive formation of  $\text{Bi}^{3-x}$  and  $\text{Bi}^0$  from  $\text{Bi}^{3+}$ . In (a), “◆” marks peaks of impurities.

$\text{Bi}^0$  in  $\text{Bi}_2\text{WO}_6$  and  $\text{BiOBr}$  (Fig. S13 and S14), indicating universality of this phenomenon in Bi-based semiconductors. To further illustrate the synergism of  $\text{Fe}^{3+}$  ions and alcohol molecules, some other metal ions were chosen to replace  $\text{Fe}^{3+}$  ions for similar synthesis. As shown by XRD patterns in Fig. 4a, the metal ions did not inhibit formation of  $\text{Bi}_2\text{MoO}_6$ , but  $\text{Co}^{2+}$  and  $\text{Cu}^{2+}$  induced generation of impurities (not discussed here). Furthermore,  $\text{Zn}^{2+}$ ,  $\text{Fe}^{3+}$ ,  $\text{Cd}^{2+}$ ,  $\text{In}^{3+}$ ,  $\text{Co}^{2+}$ , and  $\text{Ni}^{2+}$  ions with exposed d orbitals, apt to strongly coordinate with hydroxyls [28], are able to promote generation of  $\text{Bi}^0$ , as shown by distinct diffraction peaks of  $\text{Bi}^0$  in the patterns, while  $\text{K}^+$ ,  $\text{Ba}^{2+}$ ,  $\text{Na}^+$ ,  $\text{Mg}^{2+}$ , and  $\text{Al}^{3+}$  ions without exposed d orbitals, unable to strongly coordinate with hydroxyls, did not induce generation of detectable  $\text{Bi}^0$ .  $\text{Cu}^{2+}$  ions, with exposed d orbitals but the corresponding metal activity sequence,  $\text{Cu} < \text{H}$  (a lower ability of Cu in donating electrons), cannot induce generation of  $\text{Bi}^0$ , either. Based on above comprehensive analysis, it can be concluded that the strong coordination of metal ions with alcohol hydroxyls is the premise for promoting formation of Ovs and  $\text{Bi}^0$ , but the metal-hydroxyl coordination must be able to increase the electron density in alcohol molecules, i.e., enhance their reducibility (Fig. 4b), which requires the metal ions possess corresponding metal activity in front of H. Then, stepwise reduction of  $\text{Bi}^{\text{III}}$  promoted by the coordination structure would lead to generation of Ovs and even  $\text{Bi}^0$  (Fig. 4b).

### 3.2. Physicochemical properties and photocatalytic performance of $\text{Bi}^0/\text{BMO-Ov}$

Nitrogen-sorption isotherms of BMO and  $\text{B}/\text{Fe}\varphi$  all show type-IV isotherms [29] (Fig. S15a), suggesting existence of mesopores. BMO and  $\text{B}/\text{Fe}0.06$  exhibit type-H3 hysteresis loops, indicating the mesopores formed via aggregation of platelike particles, while  $\text{B}/\text{Fe}0.4$  exhibits a type-H4 hysteresis loop, indicating existence of slit-like mesopores [29]. The hysteresis loop of  $\text{B}/\text{Fe}0.2$  seems to be between type-H3 and type-H4, suggesting coexistence of platelike particle formed mesopores and slit-like mesopores, which are consistent with the SEM and TEM results. The variation of mesopore types arises from  $\text{Bi}^0$  generation induced morphological changes of hierarchical microspheres (Fig. 2a–c). BET surface areas of BMO,  $\text{B}/\text{Fe}0.06$ ,  $\text{B}/\text{Fe}0.2$ , and  $\text{B}/\text{Fe}0.4$  are determined to be 59, 115, 111, and  $57 \text{ m}^2 \text{ g}^{-1}$ , respectively, which increase then decrease with the increase of  $\varphi$ . Pore-size distribution curves of the samples (Fig. S15b) show mesopore size of 2–40 nm, and the calculated pore volume of BMO,  $\text{B}/\text{Fe}0.06$ ,  $\text{B}/\text{Fe}0.2$ , and  $\text{B}/\text{Fe}0.4$  are 0.10, 0.23, 0.14, and  $0.10 \text{ cm}^3 \text{ g}^{-1}$ , respectively, showing a sequence similar to that of the surface areas.

UV-vis diffuse reflectance spectra of BMO and  $\text{B}/\text{Fe}\varphi$  indicate new generated Ovs and  $\text{Bi}^0$  slightly enhance visible light absorption of  $\text{B}/\text{Fe}\varphi$  (Fig. S16). Photoluminescence (PL) of BMO and  $\text{B}/\text{Fe}\varphi$  weakens then strengthens with the increase of  $\varphi$ , and  $\text{B}/\text{Fe}0.2$  exhibits the lowest

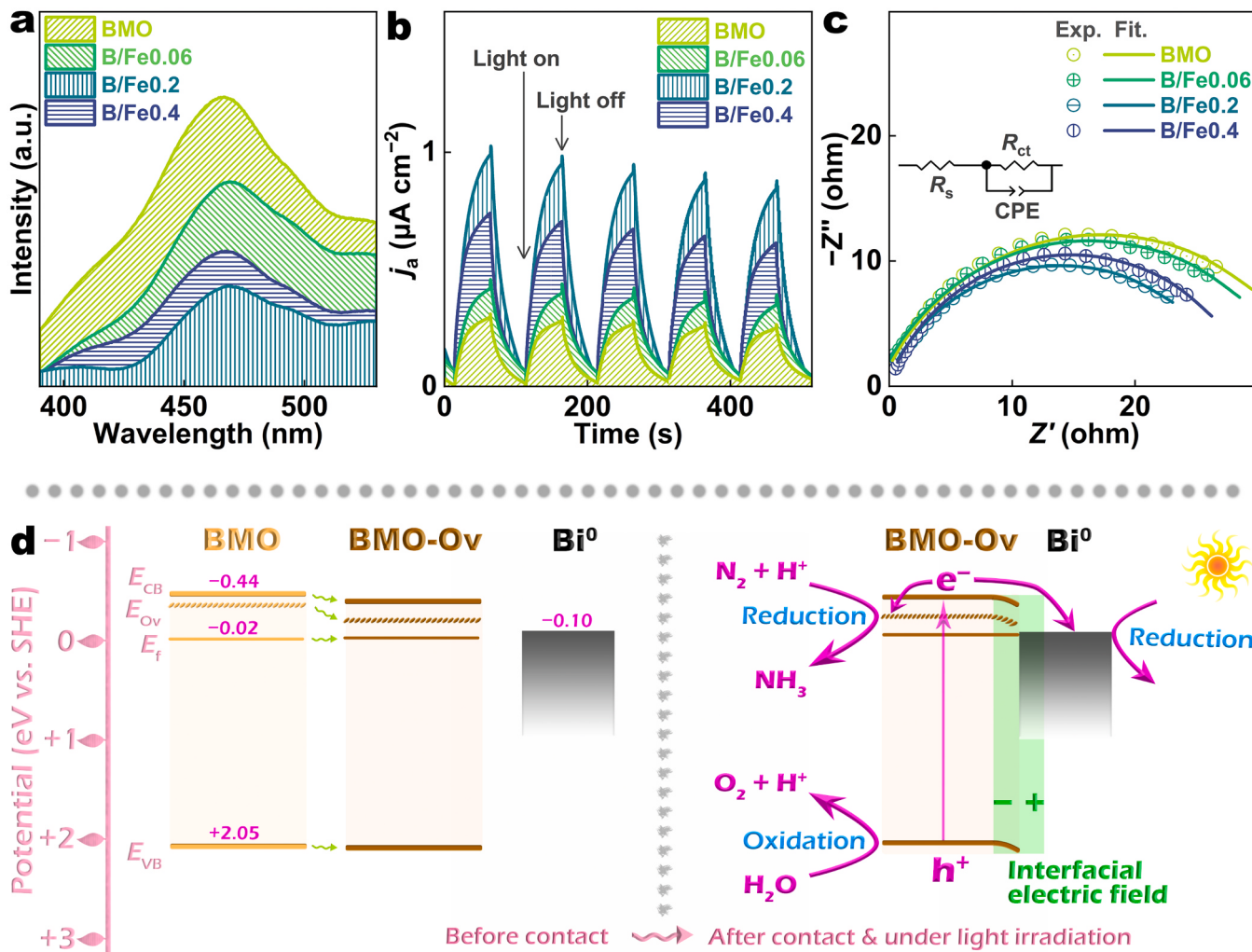


**Fig. 5.** (a) PL spectra, (b) transient photocurrent response, and (c) EIS spectra of samples; and (d) schematic illustration for energy band levels of BMO, BMO-Ov, and  $\text{Bi}^0$  and probable construction of the  $\text{Bi}^0/\text{BMO-Ov}$  heterojunction with photogenerated charge transfer pathways and PNRR mechanism shown. An equivalent circuit was provided in (c), with  $R_{\text{ct}}$ ,  $R_s$ , and CPE denoting the charge transfer resistance, the solution resistance, and the double-layer capacitance, respectively.

intensity (Fig. 5a), indicative of the lowest photogenerated charge recombination efficiency, which should benefit from the highest content of Ovs in B/Fe0.2 that can capture electrons to restrict their direct recombination with holes [12,30]. This suggests Ovs possess a higher electron-capture ability than Bi<sup>0</sup> here (if Bi<sup>0</sup> can capture electrons), considering B/Fe0.2 contains less Bi<sup>0</sup> than B/Fe0.4. Transient photocurrent response of BMO and B/Fe $\varphi$  strengthens then weakens with the increase of  $\varphi$ , and B/Fe0.2 exhibits the strongest response (Fig. 5b), indicating the highest photogenerated charge separation efficiency, consistent with the PL results. Electrochemical impedance spectroscopy (EIS) was also performed. As shown in Fig. 5c, the EIS data were fitted using the provided equivalent circuit, and obtained charge transfer resistances ( $R_{ct}$ ) of BMO, B/Fe0.06, B/Fe0.2, and B/Fe0.4 are 36.0, 34.7, 28.7, and 29.9  $\Omega$ , respectively. The variation of  $R_{ct}$ s of BMO and B/Fe $\varphi$  with the increase of  $\varphi$  is consistent with that of their PL intensity, with B/Fe0.2 exhibiting the smallest value, which manifests the highest charge transfer capability of B/Fe0.2, also favoring the efficient charge separation.

To elucidate the enhancement of photoexcited charge separation, energy band structures of Bi<sup>0</sup>/BMO-Ov were roughly determined. Energy band levels of BMO were determined in our previous work [12], and in contrast, BMO-Ov with more Ovs likely possesses a lower conduction band edge ( $E_{CB}$ ), a defect level ( $E_{Ov}$ , introduced by Ovs) further away from  $E_{CB}$ , a changeless valence band edge ( $E_{VB}$ ), and a Fermi level ( $E_f$ ) closer to the  $E_{CB}$  [12]. The work function of Bi<sup>0</sup> is about 4.34 eV [31, 32], i.e.,  $-0.10$  eV (vs. SHE), slightly higher than the  $E_f$  of BMO-Ov. As shown in Fig. 5d, after contact of BMO-Ov and Bi<sup>0</sup>, electrons transfer

from Bi<sup>0</sup> to BMO-Ov. Then, band levels of BMO-Ov move down, while that of Bi<sup>0</sup> moves up, till a unified (or equilibrium)  $E_f$  is achieved, accompanied with establishment of an interfacial electric field that induces band bending of BMO-Ov, and under light irradiation, a pseudo-equilibrium  $E_f$  is achieved [33]. These indicate both Ovs and Bi<sup>0</sup> can capture photogenerated electrons to enhance charge separation, based on close contact between Bi<sup>0</sup> and BMO-Ov (Fig. 2d). It should be noted that the electron transfer from Bi<sup>0</sup> to BMO-Ov (to achieve the unified  $E_f$ ) contributes to the shift of peaks in Bi 4f and Mo 3d XPS spectra of B/Fe0.2 to low binding energy, relative to those of BMO (Fig. 3c and d).

Given Ovs are key active sites for the photocatalytic nitrogen reduction reaction (PNRR) [34], PNRR activity of BMO and B/Fe $\varphi$  were evaluated (Fig. S17). Their average NH<sub>3</sub> production rates ( $R_N$ ) increase then decrease with the increase of  $\varphi$ , and B/Fe0.2 exhibits the greatest  $R_N$ ,  $\sim 16$  times that of BMO (Fig. 6a), with an EQY of 2.8% at 420 nm (Fig. S18) that is comparable to those of most reported photocatalysts (Table S3). The Ov-decided photoexcited charge separation capability of the samples is responsible for their PNRR activity, while the surface area is not a key factor, because B/Fe0.2 possesses a much greater  $R_N$  but a smaller surface area than B/Fe0.06, and the small photoabsorption enhancement of B/Fe0.2 (Fig. S16) is certainly also not a significant factor. Regrettably, the Ovs were often neglected upon assessing PNRR activity of “metal-doped” Bi-based compounds [8,15,35–37], though they are considered apt to form in alcoothermal synthesis of Bi-based compounds [12,38,39].

To investigate the role of Bi<sup>0</sup>, B/Fe0.2 was treated with H<sub>2</sub>O<sub>2</sub> to

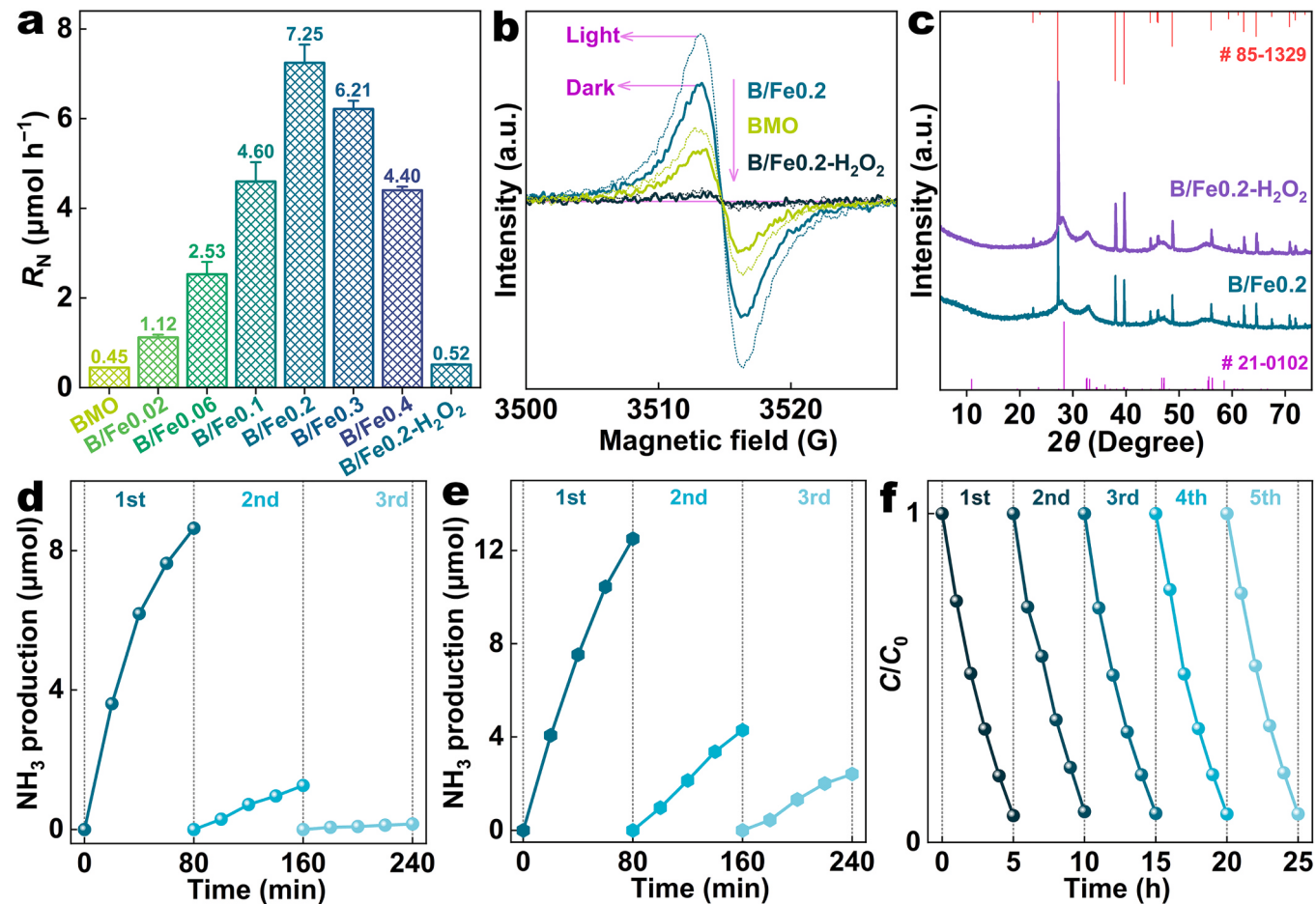


**Fig. 6.** (a) Average photocatalytic NH<sub>3</sub> production rates ( $R_N$ ) of samples in pure water under visible light irradiation; (b) EPR spectra and (c) XRD patterns of samples; cyclic PNRR experiments of B/Fe0.2 (d) in pure water and (e) in a methanol aqueous solution; and (f) the cyclic experiment of RhB photodegradation on B/Fe0.2 under visible light irradiation.

eliminate Ovs (S5, with the sample denoted as B/Fe0.2-H<sub>2</sub>O<sub>2</sub>). EPR signals of B/Fe0.2-H<sub>2</sub>O<sub>2</sub> in dark and under light irradiation almost disappear, compared with those of B/Fe0.2 and even BMO (Fig. 6b), indicating the Ovs in B/Fe0.2 were mostly eliminated by H<sub>2</sub>O<sub>2</sub> treatment. XRD patterns of B/Fe0.2-H<sub>2</sub>O<sub>2</sub> still show strong peaks, indexed to Bi<sup>0</sup> and Bi<sub>2</sub>MoO<sub>6</sub>, similarly as B/Fe0.2 (Fig. 6c), which demonstrates the H<sub>2</sub>O<sub>2</sub> treatment caused no changes of crystalline structures of Bi<sup>0</sup> and Bi<sub>2</sub>MoO<sub>6</sub>. The  $R_N$  of B/Fe0.2-H<sub>2</sub>O<sub>2</sub> is only ~7% of that of B/Fe0.2, further indicating the key role of Ovs and suggesting a negligible surface plasmonic resonance effect of Bi<sup>0</sup> [40] in contrast with the effect of Ovs in the PNRR processes, but still comparable to the  $R_N$  of BMO (Fig. 6a), though its Ov content (EPR signal) is much lower than that of BMO, which manifests Bi<sup>0</sup> also acts as the PNRR active site, though it is less effective than the Ovs here.

Moreover, the Fe-containing Bi<sub>2</sub>MoO<sub>6</sub> without Ovs and Bi<sup>0</sup>, synthesized in water (denoted as B/Fe0.2-water, S2), exhibits almost no PNRR activity (Fig. S19), suggesting Fe<sup>3+</sup> ions are not PNRR active sites. Photodegradation of RhB on BMO and B/Fe $\varphi$  was also performed and B/Fe0.2 still exhibits the highest activity (Fig. S20), benefiting from its highest photoexcited charge separation ability, with holes being the dominant active species (Fig. S21).

Photochemical stability of B/Fe0.2 was investigated via cyclic photocatalytic experiments. For the PNRR in pure water, the activity of B/Fe0.2 almost disappears after three-consecutive runs (Fig. 6d), suggesting a quite low stability of the sample, which should arise from the Ov loss caused by direct hole oxidation, according to our previous results [12,26]. Addition of methanol in the photoreaction system as a hole scavenger can prominently increase the photochemical stability of B/Fe0.2 (Fig. 6e), but cannot completely inhibit the photoactivity decrease, which differs from circumstances for Ov modified Bi<sub>2</sub>MoO<sub>6</sub> in our previous work, i.e., methanol can completely inhibit photoactivity decrease [12,26]. This difference maybe arises from that the Ov structure in B/Fe0.2 with generation of Bi<sup>0</sup> here is different from our reported Ov structures without Bi<sup>0</sup> formation [12,26], for example of probable existence of more Bi<sup>I</sup> in B/Fe0.2. In addition, the addition of methanol enhances the PNRR activity of B/Fe0.2, as shown by the first runs in Fig. 6d and e. More interestingly, B/Fe0.2 exhibits no decrease of activity in five-consecutive runs for photodegradation of RhB (Fig. 6f), indicating a very high photochemical stability. Considering holes are dominant active species for RhB degradation, i.e., RhB degradation consumes holes, and methanol oxidation in the PNRR on B/Fe0.2 also consumes holes but cannot completely inhibit the activity decrease (Fig. 6e), it can be deduced that the direct hole oxidation of Ovs in the PNRR on B/Fe0.2 may be related to chemisorption of N<sub>2</sub> at Ovs [34].

The mechanism for the PNRR on B/Fe0.2 was further investigated. In-situ Fourier transform infrared (FT-IR) spectroscopy spectra of B/Fe0.2 with adsorbed N<sub>2</sub> in the dark and under light irradiation indicate

continuous chemisorption of N<sub>2</sub> molecules on B/Fe0.2 and quick formation of NH<sub>3</sub> molecules under light irradiation, via an associative distal pathway (Fig. S22). Then, PNRR kinetic processes on BMO and BMO-Ov models (Fig. S23), based on the associative distal pathway, were comparatively investigated by DFT calculations. Reported DFT calculation results and our previous temperature-programmed desorption analyses indicate Ovs in BMO-Ov indeed favor adsorption and activation of N<sub>2</sub> molecules [12,26,41]. And a NRR pathway of (\*+N<sub>2</sub>) → \*N = NH → \*N = NH<sub>2</sub> → \*N(+NH<sub>3</sub>) → \*NH → \*NH<sub>2</sub> → (\*+NH<sub>3</sub>) (Fig. 7) is further used to research reaction kinetics on BMO and BMO-Ov. As shown in Fig. 7, the \*N = NH<sub>2</sub> → \*N(+NH<sub>3</sub>) step exhibits the greatest energy barrier for BMO (3.14 eV), suggesting this is the rate-determining step in the reaction pathway, however, this step for BMO-Ov exhibits a much smaller energy barrier (1.35 eV), suggesting the significant positive role of Ovs. For BMO-Ov, the (\*+N<sub>2</sub>) → \*N = NH step exhibits the greatest energy barrier (2.82 eV) in the pathway and is the rate-determining step, but its energy barrier is still remarkably smaller than that for BMO (3.14 eV). These results totally indicate the Ovs can accelerate the NRR kinetics via an associative distal pathway, consistent with reported results [34].

### 3.3. Analysis on Fe<sup>3+</sup> distribution in B/Fe0.2 core/shell microspheres

To confirm whether Fe<sup>3+</sup> ions dope B/Fe0.2 or not, the Fe<sup>3+</sup> distribution in the sample is well analyzed. The theoretical Fe/Bi + Mo molar ratio is 0.067, greater than the experimental value, 0.056, measured by inductively coupled plasma-optical emission spectrometry (ICP-OES), suggesting only partial Fe<sup>3+</sup> ions remain in the sample. Fe/Bi + Mo molar ratios in core/shell microspheres of B/Fe0.2, measured by EDS, are 0.083 in the shell and 0.087 in the core (Fig. 2b and e), which are close to the values obtained by XPS (0.079 for pristine B/Fe0.2 and 0.081 for Ar<sup>+</sup>-etched B/Fe0.2) (Table S2), are remarkably higher than the ICP-OES result, suggesting the Fe<sup>3+</sup> ions are not homogeneously distributed in the microspheres and mainly distribute in surface layers of the core and the shell. These probably mean that the Fe<sup>3+</sup> ions are not homogeneously doped in the nanoplates and nanosheets, and some of them may be wrapped and/or adsorbed in the surface layers (probably in the form of FeCl<sub>3</sub> and/or Fe<sub>2</sub>O<sub>3</sub>·nH<sub>2</sub>O (Fig. S24) that cannot be removed by washing), which can also be indirectly proved by residual of Cl<sup>-</sup> ions in the surface layers of microspheres in B/Fe0.2 (Fig. S12b and Table S2) that balance the charge of partial residual Fe<sup>3+</sup> ions.

Furthermore, XRD patterns of BMO and B/Fe $\varphi$  indicate gradual increase of crystal facet distance with the increase of  $\varphi$  from 0 to 0.1 (Fig. S10), suggesting the influence of Ovs dominates over the influence of possible Fe<sup>3+</sup> substitution doping (by replacing Bi<sup>III</sup>), because formation of Ovs increases the facet distance, while the Fe<sup>3+</sup> doping would result in decrease of facet distance in view of the radius of Fe<sup>3+</sup> ions

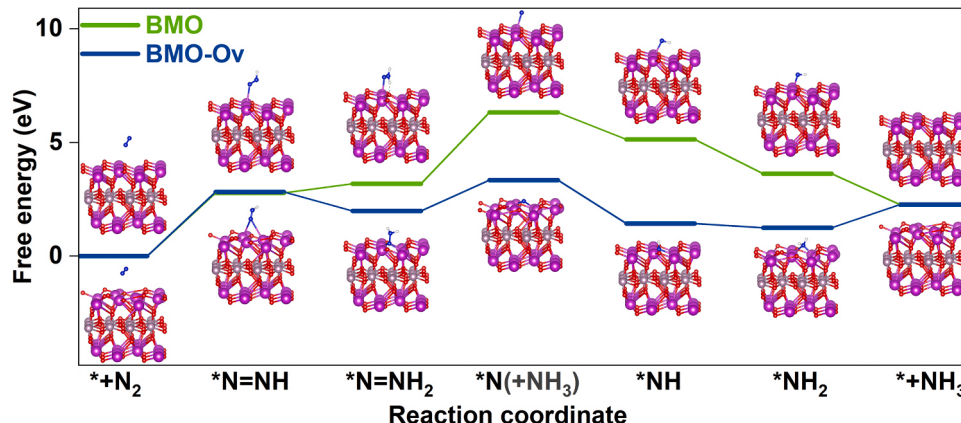


**Fig. 7.** Schematic illustration for associative distal pathways of NRRs on BMO and BMO-Ov models and corresponding reaction energy diagrams.

(64 pm) is much smaller than that of Bi<sup>III</sup> ions (108 pm). The influence of Fe<sup>3+</sup> interstitial doping may also be dominated over by that of the Ovs, because theoretically, H<sub>2</sub>O<sub>2</sub> treatment would remove the Ovs, but not induce variation of the doping Fe<sup>3+</sup> ions, whereas experimentally, H<sub>2</sub>O<sub>2</sub> treatment on B/Fe0.2 leads to decrease of crystal facet distance (Fig. S25), which should result from removal of existent Ovs. In addition, B/Fe0.2-water without Ovs exhibits no prominent shift of XRD peaks, relative to those of BMO synthesized in water (denoted as BMO-water, S2), suggesting quite low possibility for Fe<sup>3+</sup> doping in B/Fe0.2-water (Fig. S19c-f).

Overall, the possibility for substitution and interstitial doping of massive Fe<sup>3+</sup> ions in B/Fe0.2 is quite low, though doping of a handful of Fe<sup>3+</sup> ions, of which the effect is covered by the effect of Ovs, cannot be excluded. Certainly, the main active centers for the PNRR on B/Fe0.2 are not doping Fe<sup>3+</sup> ions, but the Ovs. This is different from some reported results for which doping metal ions were considered as PNRR active sites, with Ovs ignored [8,15,36,37]. In fact, the best way to investigate effects of doping metal ions on PNRR activity of metal-doped Bi-based semiconductors is to synthesize the samples in non-reductive solvents (e.g., H<sub>2</sub>O), making sure Ovs are not generated, unless the effects of Ovs can be completely ruled out.

#### 4. Conclusion

Metal-alcohol coordination was evidenced to promote reduction of Bi<sup>III</sup> in alcoothermal synthesis of Bi-based semiconductors (e.g., Bi<sub>2</sub>MoO<sub>6</sub>) to form Ovs and Bi<sup>0</sup> in Bi<sup>0</sup>/BMO-Ov. With the increase of added Fe<sup>3+</sup> amount, morphologies of Bi<sup>0</sup>/BMO-Ov change from nanoplate-composed to nanosheet-composed hierarchical microspheres; content of Ovs, surface areas, and photoexcited charge separation efficiencies increase then decrease; content of Bi<sup>0</sup> increases gradually; and photocatalytic activity increases then decreases. Bi<sup>0</sup>/BMO-Ov containing the most Ovs exhibits the highest charge separation efficiency and PNRR activity, ~16 times that of the bulk BMO, with an EQY of 2.8% at 420 nm. Ovs are the main active centers for the PNRR, though Bi<sup>0</sup> also works, while Fe<sup>3+</sup> ions should not be the active sites and even not homogeneously dope the sample. Overall, this work discloses an ignored fact that in alcoothermal synthesis of “metal doped” Bi-based compounds, metal-alcohol (e.g., Fe<sup>3+</sup>-EG) coordination may increase reducibility of alcohol molecules to promote reduction of Bi<sup>III</sup> to generate Ovs and Bi<sup>0</sup> that can enhance photogenerated charge separation, work as surface active sites, and thus photocatalytic activity.

#### CRediT authorship contribution statement

**Li Haiping:** Conceptualization, Data curation, Formal analysis, Funding acquisition, Investigation, Methodology, Writing – original draft. **Wang Guoan:** Data curation, Formal analysis, Investigation, Methodology. **Hu Wenxuan:** Methodology. **Deng Quanhua:** Methodology, Writing – review & editing. **Hou Wanguo:** Funding acquisition, Writing – review & editing.

#### Declaration of Competing Interest

The authors declare that they have no known competing financial interests or personal relationships that could have appeared to influence the work reported in this paper.

#### Data availability

Data will be made available on request.

#### Acknowledgments

This work was supported by the National Natural Science Foundation of China (No. 22272088). We thank the Center for Structural and

Property Analysis of Shandong University and Shiyanjia Lab ([www.shianjia.com](http://www.shianjia.com)) for their assistance in characterizations of samples.

#### Appendix A. Supporting information

Supplementary data associated with this article can be found in the online version at doi:[10.1016/j.apcatb.2023.123652](https://doi.org/10.1016/j.apcatb.2023.123652).

#### References

- [1] N. Tian, C. Hu, J. Wang, Y. Zhang, T. Ma, H. Huang, Layered bismuth-based photocatalysts, *Coord. Chem. Rev.* 463 (2022), 214515, <https://doi.org/10.1016/j.ccr.2022.214515>.
- [2] H.B. Yu, L.B. Jiang, H. Wang, B.B. Huang, X.Z. Yuan, J.H. Huang, J. Zhang, G. M. Zeng, Modulation of Bi<sub>2</sub>MoO<sub>6</sub>-based materials for photocatalytic water splitting and environmental application: a critical review, *Small* 15 (2019), e1901008, <https://doi.org/10.1002/smll.201901008>.
- [3] N. Zhang, R. Ciriminna, M. Pagliaro, Y.J. Xu, Nanochemistry-derived Bi<sub>2</sub>WO<sub>6</sub> nanostructures: towards production of sustainable chemicals and fuels induced by visible light, *Chem. Soc. Rev.* 43 (2014) 5276–5287, <https://doi.org/10.1039/c4cs00056k>.
- [4] X. Dong, Z. Cui, X. Shi, P. Yan, Z. Wang, A.C. Co, F. Dong, Insights into dynamic surface bromide sites in Bi<sub>4</sub>O<sub>5</sub>Br<sub>2</sub> for sustainable N<sub>2</sub> photofixation, *Angew. Chem. Int. Ed.* 61 (2022), e202200937, <https://doi.org/10.1002/anie.202200937>.
- [5] J. Wu, X. Li, W. Shi, P. Ling, Y. Sun, X. Jiao, S. Gao, L. Liang, J. Xu, W. Yan, C. Wang, Y. Xie, Efficient visible-light-driven CO<sub>2</sub> reduction mediated by defect-engineered BiOBr atomic layers, *Angew. Chem. Int. Ed.* 57 (2018) 8719–8723, <https://doi.org/10.1002/anie.201803514>.
- [6] J. Di, J.X. Xia, Y.P. Ge, L. Xu, H. Xu, M.Q. He, Q. Zhang, H.M. Li, Reactable ionic liquid-assisted rapid synthesis of BiOI hollow microspheres at room temperature with enhanced photocatalytic activity, *J. Mater. Chem. A* 2 (2014) 15864–15874, <https://doi.org/10.1039/c4ta02400a>.
- [7] J. Sun, X. Li, Q. Zhao, B. Liu, Ultrathin nanoflake-assembled hierarchical BiOBr microflower with highly exposed {001} facets for efficient photocatalytic degradation of gaseous ortho-dichlorobenzene, *Appl. Catal. B* 281 (2021), 119478, <https://doi.org/10.1016/j.apcatb.2020.119478>.
- [8] Q. Meng, C. Lv, J. Sun, W. Hong, W. Xing, L. Qiang, G. Chen, X. Jin, High-efficiency Fe-Mediated Bi<sub>2</sub>MoO<sub>6</sub> nitrogen-fixing photocatalyst: reduced surface work function and ameliorated surface reaction, *Appl. Catal. B* 256 (2019), 117781, <https://doi.org/10.1016/j.apcatb.2019.117781>.
- [9] Z. Jin, J. Li, Y. Zhang, D. Liu, H. Ding, B.B. Mamba, A.T. Kuvarega, J. Gui, Rational design of efficient visible-light photocatalysts (1D@2D/0D) ZnO@Ni-doped BiOBr/Bi heterojunction: considerations on hierarchical structures, doping and SPR effect, *J. Mater. Sci. Technol.* 125 (2022) 38–50, <https://doi.org/10.1016/j.jmst.2022.01.034>.
- [10] H. Yu, D. Ge, Y. Liu, Y. Lu, X. Wang, M. Huo, W. Qin, One-pot synthesis of BiOCl microflowers co-modified with Mn and oxygen vacancies for enhanced photocatalytic degradation of tetracycline under visible light, *Sep. Purif. Technol.* 251 (2020), 117414, <https://doi.org/10.1016/j.seppur.2020.117414>.
- [11] X. Chen, J. Liu, H. Wang, Y. Ding, Y. Sun, H. Yan, One-step approach to novel Bi<sub>4</sub>V<sub>2</sub>O<sub>11</sub> hierarchical hollow microspheres with high visible-light-driven photocatalytic activities, *J. Mater. Chem. A* 1 (2013) 877–883, <https://doi.org/10.1039/C2TA00312K>.
- [12] G. Wang, T. Huo, Q. Deng, F. Yu, Y. Xia, H. Li, W. Hou, Surface-layer bromine doping enhanced generation of surface oxygen vacancies in bismuth molybdate for efficient photocatalytic nitrogen fixation, *Appl. Catal. B* 310 (2022), 121319, <https://doi.org/10.1016/j.apcatb.2022.121319>.
- [13] H. Li, J. Shang, Z. Ai, L. Zhang, Efficient visible light nitrogen fixation with BiOBr nanosheets of oxygen vacancies on the exposed 001 facets, *J. Am. Chem. Soc.* 137 (2015) 6393–6399, <https://doi.org/10.1021/jacs.5b03105>.
- [14] F. Rao, G. Zhu, M. Hojaberdi, W. Zhang, S. Li, J. Gao, F. Zhang, Y. Huang, Y. Huang, Uniform Zn<sup>2+</sup>-doped BiOI microspheres assembled by ultrathin nanosheets with tunable oxygen vacancies for super-stable removal of NO, *J. Phys. Chem. C* 123 (2019) 16268–16280, <https://doi.org/10.1021/acs.jpcc.9b03961>.
- [15] Z. Shen, F. Li, J. Lu, Z. Wang, R. Li, X. Zhang, C. Zhang, Y. Wang, Y. Wang, Z. Lv, J. Liu, C. Fan, Enhanced N<sub>2</sub> photofixation activity of flower-like BiOCl by in situ Fe (III) doped as an activation center, *J. Colloid Interface Sci.* 584 (2021) 174–181, <https://doi.org/10.1016/j.jcis.2020.09.111>.
- [16] T. Zhang, S. Zhang, C. Wu, H. Zuo, Q. Yan, Novel La<sup>3+</sup>/Sm<sup>3+</sup> co-doped Bi<sub>5</sub>O<sub>7</sub>I with efficient visible-light photocatalytic activity for advanced treatment of wastewater: internal mechanism, TC degradation pathway, and toxicity analysis, *Chemosphere* 313 (2023), 137540, <https://doi.org/10.1016/j.chemosphere.2022.137540>.
- [17] Y. Liu, Z. Hu, J.C. Yu, Fe enhanced visible-light-driven nitrogen fixation on BiOBr nanosheets, *Chem. Mater.* 32 (2020) 1488–1494, <https://doi.org/10.1021/acs.chemmater.9b04448>.
- [18] C. Guan, T. Hou, W. Nie, Q. Zhang, L. Duan, X. Zhao, Enhanced photocatalytic reduction of CO<sub>2</sub> on BiOBr under synergistic effect of Zn doping and induced oxygen vacancy generation, *J. Colloid Interface Sci.* 633 (2023) 177–188, <https://doi.org/10.1016/j.jcis.2022.11.106>.
- [19] D. Xu, H. Feng, Y. Dong, Q. Wang, G. Zhang, L. Lv, Z. Ren, P. Wang, Enhanced molecular oxygen activation on (001) facets of Zn-doped BiOCl nanosheets for ciprofloxacin degradation, *Adv. Mater. Interfaces* 7 (2020), 2000548, <https://doi.org/10.1002/admi.202000548>.

[20] H. Li, Q. Deng, J. Liu, W. Hou, N. Du, R. Zhang, X. Tao, Synthesis, characterization and enhanced visible light photocatalytic activity of  $\text{Bi}_2\text{MoO}_6/\text{Zn-Al}$  layered double hydroxide hierarchical heterostructures, *Catal. Sci. Technol.* 4 (2014) 1028–1037, <https://doi.org/10.1039/c3cy00940h>.

[21] Y. Zhang, X. Zhi, J.R. Harmer, H. Xu, K. Davey, J. Ran, S.-Z. Qiao, Facet-specific active surface regulation of  $\text{Bi}_x\text{MO}_y$  ( $M=\text{Mo, V, W}$ ) nanosheets for boosted photocatalytic  $\text{CO}_2$  reduction, *Angew. Chem. Int. Ed.* 61 (2022), e202212355, <https://doi.org/10.1002/anie.202212355>.

[22] Z. Hao, X. Shi, W. Zhu, X. Zhang, Z. Yang, L. Li, Z. Hu, Q. Zhao, S. Chou, Bismuth nanoparticles embedded in a carbon skeleton as an anode for high power density potassium-ion batteries, *Chem. Sci.* 13 (2022) 11376–11381, <https://doi.org/10.1039/D2SC04217G>.

[23] Y. Quan, M.H.N. YiO, Y. Li, R.J. Myers, A. Kafizas, Influence of Bi co-catalyst particle size on the photocatalytic activity of BiOI microflowers in Bi/BiOI junctions - a mechanistic study of charge carrier behaviour, *J. Photochem. Photobiol. A* 443 (2023), 114889, <https://doi.org/10.1016/j.jphotochem.2023.114889>.

[24] X. Xie, Q.-U. Hassan, H. Lu, F. Rao, J. Gao, G. Zhu, In situ construction of oxygen-vacancy-rich  $\text{Bi}^0@\text{Bi}_2\text{WO}_{6-x}$  microspheres with enhanced visible light photocatalytic for NO removal, *Chin. Chem. Lett.* 32 (2021) 2038–2042, <https://doi.org/10.1016/j.cclet.2020.10.002>.

[25] J. Zheng, Z. Xu, S. Xin, B. Zhu, L. Nie, Generation of singlet oxygen over  $\text{CeO}_2/\text{K}$ , Na-codoped g-C<sub>3</sub>N<sub>4</sub> for tetracycline hydrochloride degradation over a wide pH range, *Dalton Trans.* 51 (2022) 12883–12894, <https://doi.org/10.1039/D2DT01748B>.

[26] G. Wang, Q. Deng, H. Li, W. Hou, Mannitol and acidity co-tuned synthesis of oxygen-vacancy-modified bismuth molybdate nanorods for efficient photocatalytic nitrogen reduction to ammonia, *Sci. China Mater.* 66 (2023) 1435–1446, <https://doi.org/10.1007/s40843-022-2291-7>.

[27] W.J. Dong, I.A. Navid, Y. Xiao, T.H. Lee, J.W. Lim, D. Lee, H.W. Jang, J.-L. Lee, Z. Mi, Bi catalysts supported on GaN nanowires toward efficient photoelectrochemical  $\text{CO}_2$  reduction, *J. Mater. Chem. A* 10 (2022) 7869–7877, <https://doi.org/10.1039/D2TA00032F>.

[28] W. Zhou, R. Saran, J. Liu, Metal sensing by DNA, *Chem. Rev.* 117 (2017) 8272–8325, <https://doi.org/10.1021/acs.chemrev.7b00063>.

[29] M. Kruk, M. Jaroniec, Gas adsorption characterization of ordered organic–inorganic nanocomposite materials, *Chem. Mater.* 13 (2001) 3169–3183, <https://doi.org/10.1021/cm0101069>.

[30] Y. Mao, P. Wang, L. Li, Z. Chen, H. Wang, Y. Li, S. Zhan, Unravelling the synergy between oxygen vacancies and oxygen substitution in  $\text{BiO}_{2-x}$  for efficient molecular-oxygen activation, *Angew. Chem. Int. Ed.* 59 (2020) 3685–3690, <https://doi.org/10.1002/anie.201914001>.

[31] T. Nyberg, An alternative method to build organic photodiodes, *Synth. Met.* 140 (2004) 281–286, [https://doi.org/10.1016/S0379-6779\(03\)00375-8](https://doi.org/10.1016/S0379-6779(03)00375-8).

[32] J.D. Smith, 21 - Arsenic, antimony and bismuth, in: J.C. Bailar, H.J. Emeléus, R. Nyholm, A.F. Trotman-Dickenson (Eds.), *Comprehensive Inorganic Chemistry*, Pergamon, Oxford, 1973, p. 558.

[33] H. Li, G. Ba, Z. Liang, Q. Deng, W. Hou, Construction of direct all-solid-state Z-scheme p-n copper indium disulfide/tungsten oxide heterojunction photocatalysts: function of interfacial electric field, *J. Colloid Interface Sci.* 555 (2019) 72–81, <https://doi.org/10.1016/j.jcis.2019.07.073>.

[34] P. Li, Z. Zhou, Q. Wang, M. Guo, S. Chen, J. Low, R. Long, W. Liu, P. Ding, Y. Wu, Y. Xiong, Visible-light-driven nitrogen fixation catalyzed by  $\text{Bi}_5\text{O}_7\text{Br}$  nanostructures: enhanced performance by oxygen vacancies, *J. Am. Chem. Soc.* 142 (2020) 12430–12439, <https://doi.org/10.1021/jacs.0c05097>.

[35] Y. Huang, Y. Zhu, S. Chen, X. Xie, Z. Wu, N. Zhang, Schottky junctions with Bi cocatalyst for taming aqueous phase  $\text{N}_2$  reduction toward enhanced solar ammonia production, *Adv. Sci. S.* 8 (2021), 2003626, <https://doi.org/10.1002/advs.202003626>.

[36] Z. Liu, X. Li, S. Su, W. Ding, L. Meng, Y. Wang, M. Tan, M. Luo, Enhancing photocatalytic nitrogen fixation performance of Co-doped bismuth molybdate through band engineering tuning, *Appl. Surf. Sci.* 611 (2023), 155627, <https://doi.org/10.1016/j.apsusc.2022.155627>.

[37] T. Ma, C. Yang, L. Guo, R.A. Soomro, D. Wang, B. Xu, F. Fu, Refining electronic properties of  $\text{Bi}_2\text{MoO}_6$  by In-doping for boosting overall nitrogen fixation via relay catalysis, *Appl. Catal. B* 330 (2023), 122643, <https://doi.org/10.1016/j.apcatb.2023.122643>.

[38] X. Yang, S. Wang, N. Yang, W. Zhou, P. Wang, K. Jiang, S. Li, H. Song, X. Ding, H. Chen, J. Ye, Oxygen vacancies induced special  $\text{CO}_2$  adsorption modes on  $\text{Bi}_2\text{MoO}_6$  for highly selective conversion to  $\text{CH}_4$ , *Appl. Catal. B* 259 (2019), 118088, <https://doi.org/10.1016/j.apcatb.2019.118088>.

[39] X. Chen, X. Zhang, Y.-H. Li, M.-Y. Qi, J.-Y. Li, Z.-R. Tang, Z. Zhou, Y.-J. Xu, Transition metal doping  $\text{BiOBr}$  nanosheets with oxygen vacancy and exposed {102} facets for visible light nitrogen fixation, *Appl. Catal. B* 281 (2021), 119516, <https://doi.org/10.1016/j.apcatb.2020.119516>.

[40] F. Dong, Q. Li, Y. Sun, W.-K. Ho, Noble metal-like behavior of plasmonic Bi particles as a cocatalyst deposited on  $(\text{BiO})_2\text{CO}_3$  microspheres for efficient visible light photocatalysis, *ACS Catal.* 4 (2014) 4341–4350, <https://doi.org/10.1021/cs501038q>.

[41] G. Li, W. Yang, S. Gao, Q. Shen, J. Xue, K. Chen, Q. Li, Creation of rich oxygen vacancies in bismuth molybdate nanosheets to boost the photocatalytic nitrogen fixation performance under visible light illumination, *Chem. Eng. J.* 404 (2021), 127115, <https://doi.org/10.1016/j.cej.2020.127115>.